Article

# Influence of Nanoarchitecture on Charge Donation and the Electrical-Transport Properties in $[(SnSe)_{1+\delta}][TiSe_2]_q$ Heterostructures

Danielle M. Hamann, Dylan Bardgett, Sage R. Bauers, Thomas W. Kasel, Austin M. Mroz, Christopher H. Hendon, Douglas L. Medlin, and David C. Johnson*

Read Online

ACCESS | Metrics & More | Article Recommendations | Supporting Information

**ABSTRACT:** A series of $[(SnSe)_{1+\delta}][TiSe_2]_q$ heterostructures with systematic changes in the number of $TiSe_2$ layers in the repeating unit were synthesized, and both the structure and electronic-transport properties were characterized. The $c$-axis lattice parameter increased linearly as $q$ increased, and the slope was consistent with the thickness of a $TiSe_2$ layer. In-plane lattice constants for SnSe and $TiSe_2$ were independent of $q$. Temperature-dependent resistivity and Hall coefficient data varied systematically as $q$ was increased. The low-temperature electrical data was modeled assuming that only electrons were involved, and the data was fit to a variable range hopping mechanism. The number of carriers involved in this low-temperature transport decreased as $q$ increased, indicating that approximately 1/10th of an electron per SnSe bilayer was transferred to the $TiSe_2$. Calculations also indicated that there was charge donation from the SnSe layer to the $TiSe_2$ layer, resulting in an ionic bond between the layers, which aided in stabilizing the heterostructures. The charge donation created a $TiSe_2-SnSe-TiSe_2$ block with the properties distinct from the constituent bulk properties. At high temperatures in large $q$ samples, the transport data required holes to be activated across a band gap to be successfully modeled. This high-temperature transport scales with the number of $TiSe_2$ layers that are not adjacent to SnSe. Using a consistent model across all of the samples significantly constrained the adjustable parameters. The charge transfer between the two constituents results in the stabilization of the heterostructure by an ionic interaction and the formation of a conducting $TiSe_2-SnSe-TiSe_2$ block. This is consistent with prior reports, where interactions between two-dimensional (2D) layers and their surroundings (i.e., adjacent layers, substrate, or atmosphere) have been shown to strongly influence the properties.
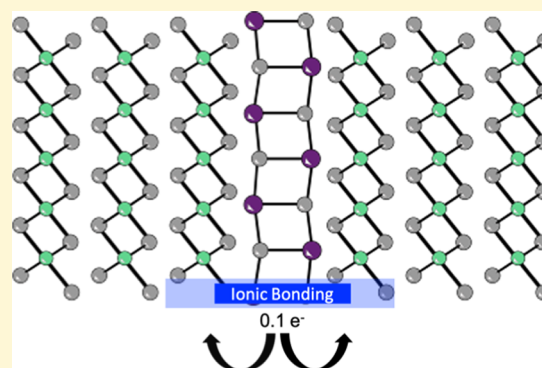
While the ability to isolate graphene and other two-dimensional (2D) materials has been known since the 1970s, the discovery of an easy optical method to determine the thickness of these thin materials has facilitated an explosion of research activity.[1] Researchers have discovered a number of unusual emergent properties, especially at the monolayer limit, including the conversion of indirect to direct band gaps,[2,3] the observation of the fractional quantum Hall effect,[4] the realization of Hofstadter's butterfly,[5−7] and advances in valleytronics.[8] Researchers also discovered that "artificial" materials created by stacking different 2D layers in designed sequences have emergent properties and provide many experimental parameters (identity, properties, thickness, and sequence of layers) that can be used to modify and manipulate these properties.[9−12] The interaction between a 2D layer and a substrate or a neighboring 2D layer in heterostructures has been found to strongly impact the emergent electronic properties.[13,14] The atomically flat interfaces between adjacent surfaces provide a large area where the orbitals extending from each layer overlap and interact, resulting in a significant renormalization of the electronic states. Due to the easy cleaving of the bulk materials along these crystal planes, the

interactions between the layers have typically been described as weak van der Waals interactions, but the substrate-dependent properties suggest that stronger interactions are present. Understanding the interaction between layers and the impact of these interactions on the near Fermi energy electronic structure is critical to understand the evolution of emergent properties—a critical step in designing the heterostructures for next-generation devices.

There is significant evidence indicating that the common assumption of weak van der Waals bonding between layers in a heterostructure is incorrect. Perhaps, the strongest piece of evidence for stronger interactions between layers in a heterostructure is the thermodynamic stability of the misfit layer compounds, compounds that contain alternating bilayers

of a rock salt structure and a monolayer or bilayer of a transition-metal dichalcogenide. These compounds are formed via direct reaction of the elements, such as Ti, Se, and Sn, at high temperatures for long time periods.[15] The literature describes the bonding between the layers in these compounds as weak when the cation in the rock salt layer is divalent.[16−18] For these compounds to be thermodynamically stable, however, the bonding between the rock salt-structured bilayer and the dichalcogenide layer must be stronger than the sum of the ionic interaction within the bulk rock salt structure and the bonding between the layers in the bulk dichalcogenide. A significant interaction between the layers of a heterostructure that is often ignored is charge transfer. Since the chemical potential and dielectric constants of the various constituent layers will be dissimilar, the spatial extent, energies, and occupancy of these wave functions will be different in the heterostructure compared to their isolated layers. The resulting charge transfer, a fraction of an electron per formula unit of the constituents, can create a strong "ionic bond" across the interface that stabilizes these compounds.[19] This charge transfer can have a dramatic effect on the properties, such as emergent superconductivity of $(SnSe)_{1.18}(TiSe_2)_2$.[15]

In this paper, a series of $[(SnSe)_{1+\delta}][TiSe_2]_q$ heterostructures are synthesized to quantify the amount of charge transfer and probe the importance of charge transfer on the evolution of the electrical properties as a function of layer thickness. This system was chosen because the electrical properties of $TiSe_2$ and misfit compounds containing $TiSe_2$ layers are well studied and known to be very sensitive to variations in carrier concentration, specific dopants, defect concentrations, and constituent structures.[15,20−24] $TiSe_2$ has been reported to have a charge density wave, to be a heavily doped semiconductor, and is theoretically calculated to be a semiconductor with a small band gap if made defect free.[20,25−27] SnSe has been reported to be a semiconductor, a promising thermoelectric material, and a topological crystalline material.[28−30] The 1−1 misfit compound has regions of rotational disorder and is a normal metal, while the 1−2 misfit layer compound is superconducting.[15,23,31] In the $[(SnSe)_{1+\delta}]_m[TiSe_2]_1$ homologous series of compounds, an unusual change in the electronic properties was reported.[24] Here, we prepared and structurally characterized the $q = 1-4, 6, 8, 11$, and 15 heterostructures, which all contain a single SnSe layer separated by $q$ layers of $TiSe_2$. Though varying from their bulk counterparts, the constituent crystal structures do not change with nanoarchitecture. The electrical properties systematically evolve as $q$ increases. The changes were successfully modeled based on a $[(SnSe)_{1+\delta}][TiSe_2]_2$-conducting unit that becomes increasingly isolated by the $TiSe_2$ layers as $q$ becomes larger. As the number of the $TiSe_2$ layers increases, the average carrier concentration decreases, and there is increasing localization of the carriers in the $[(SnSe)_{1+\delta}][TiSe_2]_2$ at low temperatures consistent with Anderson localization. In heterostructures with large $q$ values, additional carriers (electrons and holes) are created by thermal excitation at higher temperatures. Density functional theory (DFT) calculations and the modeling of electrical data both indicate charge transfer of approximately 0.1 electron per SnSe to $TiSe_2$. Quantifying the charge transfer between layers and understanding how it changes with nanoarchitecture is important for the future design of thin-film materials with targeted properties.

## METHODS AND MATERIALS

Samples were prepared via the MER method as described previously by Atkins and co-workers.[32,33] Elemental layers were deposited onto Si with a native $SiO_2$ layer and quartz substrate for structural and electrical characterizations, respectively. Titanium and tin (Alfa Aeser, 99.99 and 99.98%, respectively) were deposited using electron beam guns, while selenium (Alfa Aeser, 99.999%) was deposited using a Knudson effusion cell. Quartz crystal microbalances, located between the source and the substrate, were used to monitor the deposition rate and thickness of each element. Custom software, which communicated with the crystals and controlled the pneumatic shutters, assembled the precursor with the designed architecture, and the number of atoms per elemental layer was calculated to produce the targeted product.[34]

Samples were annealed on a hotplate at 350 °C for 30 min in a nitrogen atmosphere with less than 1 ppm oxygen. This temperature was determined in a previous study of $[(SnSe)_{1.2}]_1[TiSe_2]_1$ samples and assumed to be the optimal annealing temperature for these $[(SnSe)_{1+\delta}]_1[TiSe_2]_q$ heterostructures.[31] The annealed structures were determined via X-ray diffraction (XRD) using Cu K$\alpha$ radiation ($\lambda$ = 0.15418 nm). Total film and repeating unit ($c$-axis lattice parameter) thicknesses were gathered from low-angle X-ray reflectivity (XRR) and specular diffraction data, respectively. The reflectivity and specular diffraction data were collected on a Bruker D8-Discover diffractometer using a locked couple scan type and ($\theta-2\theta$) ranges of 0−10 and 5−65°, respectively. The in-plane diffraction scans were collected using a Rigaku Smartlab diffractometer with a ($\theta-2\theta$) range of 15−110°.

Ultrathin cross sections were prepared using an FEI Helios Nanolab 600i focused ion beam scanning electron microscope (FIB-SEM) for electron microscopy investigations. As the lamellae approached electron transparency, low-energy 2 kV milling was used to avoid damaging the crystallinity of the sample while thinning the sample to the targeted thickness. The prepared samples were imaged in high-angle annular dark-field scanning transmission electron microscopy (HAADF-STEM) mode at 300 kV using a Thermofisher Themis TEM located at the Sandia National Laboratory in Livermore, CA.

Temperature-dependent transport measurements were collected on a home-built measurement system that uses a closed-cycle helium cryostat to obtain low temperatures. Resistivity measurements were conducted using the van der Pauw technique. Films were deposited onto a masked quartz substrate to create 1 cm × 1 cm samples with a cross-arm geometry. Indium contacts were pressed onto each of the four points of the cross. Resistivity measurements were taken periodically at temperatures ranging from 20 to 295 K. Hall measurements were done with magnetic fields ranging from 0 to 16 kG also using the van der Pauw technique. At 4 kG increments, a constant current of 0.100 A was sequentially applied to each of the four lead configurations. The Hall coefficient was determined from the slope of a linear fit of the Hall voltage as a function of the magnetic field. Seebeck measurements were performed on a rectangular sample deposited onto a quartz substrate. One end of the sample was cooled, and the temperature difference was measured using independent thermocouples. The voltage difference between either end of the sample was measured and divided by the temperature difference to obtain the Seebeck coefficient.

Computational models of bulk SnSe and $TiSe_2$ were prepared from the computationally ready structures from the Materials Project.[35] Prior to the generation of slab and heterojunction models, the bulk structures were geometrically optimized. All calculations utilized the PBEsol functional[36,37] with Tkatchenko−Scheffler dispersion corrections[38] and a scaling factor of 0.94 alongside a projector-augmented wave (PAW) basis[39] and a 500 eV plane-wave cutoff as implemented in the Vienna Ab initio Simulation Package (VASP).[40−43] All structures were considered geometrically optimized when forces were below 0.005 eV/Å$^2$ and electronically optimized when the total energy was below $10^{-6}$ eV. A 10 × 10 × 4 Γ-centered $k$-grid was used for both bulk SnSe and bulk $TiSe_2$. Once bulk models were

geometrically optimized, slab models were generated containing seven layers and ~20 Å of vacuum space with a Γ-centered $k$-mesh of $10 \times 10 \times 1$ for both SnSe and TiSe$_2$. The density of state plots of the slab models were calculated from a minimized wave function using the same electronic convergence criteria as above and Gaussian smearing with $\sigma = 0.3$ eV with a $10 \times 10 \times 1$ and a $6 \times 6 \times 1$ Γ-centered $k$-grid for SnSe and TiSe$_2$, respectively. The valence band maximum eigenvalue was aligned to vacuum utilizing the MacroDensity code.[44,45] While a previous report on the SnSe−TiSe$_2$ heterojunction utilized an island-based modeling approach,[23] here we elected to utilize supercell expansions of the bulk models to maintain the $ab$ plane connectivity as to not artificially confine SnSe. This was done by first generating a $6 \times 7 \times 2$ supercell of TiSe$_2$ followed by the removal of one of the two TiSe$_2$ sheets to create a cavity for SnSe insertion. SnSe was expanded to a $5 \times 6 \times 1$ supercell, and a single layer was inserted into the TiSe$_2$ cavity. The heterointerface was then formed by manually placing the SnSe layer over the TiSe$_2$ layer. This procedure could also be performed using automation and would yield the same geometry.[46] The computational cif files containing the PBEsol-optimized computational structures are included as the Supporting Information (SI) materials. The SnSe layer was subsequently rotated about the normal of the $ab$ plane by hand to minimize lattice mismatch. Following rotation, excess atoms were removed. The resulting heterojunction was geometrically minimized using the criteria above in a spin-polarized scheme with a $2 \times 2 \times 2$ Γ-centered $k$-grid. After geometric optimization, Bader charge analysis was performed on both the heterojunction and bulk models using the Bader code and the charge density was sampled with 150% of the default resolution in all directions.[47−49]

## RESULTS AND DISCUSSION

A series of $[(SnSe)_{1+\delta}]_1[TiSe_2]_q$ heterostructures with an increasing number of TiSe$_2$ layers per repeat unit ($1 \leq q \leq 15$) were prepared from precursors with composition profiles designed to mimic the desired final product. Each precursor was made by depositing the elemental layers in a repeating sequence containing a single Sn|Se bilayer and $q$ Ti|Se bilayers. The deposition parameters for the Sn|Se bilayer were adjusted to obtain a 1 to 1 atomic ratio of Sn to Se and the required number of atoms such that two 001 planes of rock salt-structured SnSe formed from the deposited bilayers when annealed. The deposition parameters for the Ti|Se bilayer were adjusted to obtain a 1 to 2 ratio of Ti to Se and a thickness such that a single TiSe$_2$ layer with a CdI$_2$ structure formed upon annealing. The heterostructures with $q = 1, 2, 3, 4, 6, 8, 11,$ and 15 were targeted by changing the number of Ti|Se bilayers within the repeating unit. The Sn|Se + $q$[Ti|Se] sequence of layers was repeated 41, 28, 21, 17, 12, 9, 7, and 5 times, respectively, to form precursor films that were approximately 50 nm thick. Annealing at 350 °C for 30 min converted the designed precursors into the targeted heterostructures, as reported previously for $[(SnSe)_{1+\delta}]_1[TiSe_2]_1$ and $[(SnSe)_{1+\delta}]_m[TiSe_2]_1$ compounds.[24,31]

Figure 1 contains X-ray reflectivity (XRR) patterns of the annealed $q = 1, 2, 4,$ and 6 samples. The patterns contain Kiessig fringes from the interference between the front and the back of the samples and Bragg reflections from the repeating layer sequence. The angle of the first-order Bragg reflection systematically decreases as the number of TiSe$_2$ layers increases, consistent with an increasing $c$-axis lattice parameter. The $q = 1, 2, 4,$ and 6 compounds have 38, 24, 14, and 10 Kiessig fringes between Bragg reflections, respectively, indicating that the total thickness contains 40, 26, 16, and 12 unit cells in the final product. The number of unit cells in the $q = 6$ sample matches the number of layers that were deposited in the precursor. The number of unit cells for the $q = 1$ and 4
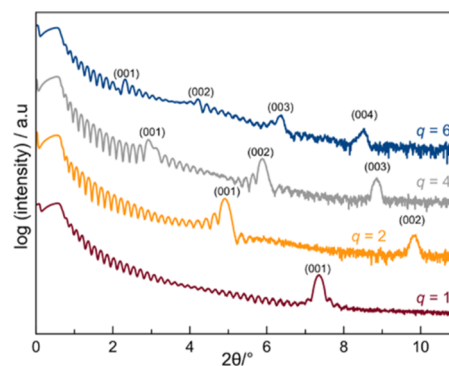


**Figure 1.** XRR patterns of the representative $[(SnSe)_{1+\delta}][TiSe_2]_q$ heterostructures after low-temperature annealing. The $(00l)$ Bragg reflections are indexed and are different from the low-intensity maxima between the Bragg reflections known as Kiessig fringes that are due to the finite thickness of the films.

samples is 1 less than deposited in the precursor. For the $q = 2$, there are two fewer unit cells in the annealed sample than deposited in the precursor. The variations in the XRR patterns demonstrating the change in the total number of layers can be observed in Figure S1. The decrease in the number of unit cells relative to the number of layers deposited in the precursor for these samples results from deviation in the amount of the material deposited compared to the target amount of the material needed in each repeating unit, the reaction of the first layer(s) with the substrate, and/or surface oxidation of the film during annealing. The angle where the Kiessig fringes disappear is related to the roughness of the films via the Parratt equation.[50] Most of the fringes can no longer be resolved at ~6° $2\theta$ for all of the samples, indicating a roughness less than ~0.4 nm. The presence of Bragg reflections in the XRR patterns of the annealed samples parallels those observed in the as-deposited samples, indicating that the nanoarchitecture of the precursors is preserved as the desired heterostructures self-assemble (Figure S1).

Specular X-ray diffraction scans were collected on each of the $[(SnSe)_{1+\delta}]_1[TiSe_2]_q$ heterostructures and are shown in Figure 2. The intensity maxima in each pattern can all be indexed as $(00l)$ reflections, indicating that the heterostructures are crystallographically aligned to the substrate. With increasing $q$, the spacing between observed Bragg reflections
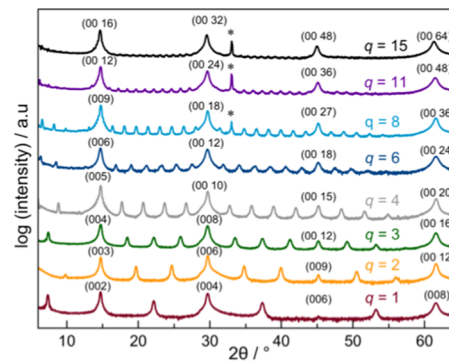


**Figure 2.** Specular diffraction patterns of the $[(SnSe)_{1+\delta}][TiSe_2]_q$ heterostructures. All reflections can be indexed as $(00l)$ Bragg reflections and indices for select reflections are indicated in the pattern. The asterisk marks a Si reflection from the substrate present in particular patterns.

decreases as the $c$-axis lattice parameter increases. The intensities of most reflections diminish as $q$ increases except for the reflections at approximately 14, 30, and 62° $2\theta$, which become more intense. More of the Fourier terms are needed to describe the structure as the number of $\sim$0.6 nm thick $TiSe_2$ layers is increased. The calculated $c$-axis lattice parameters for the $[(SnSe)_{1+\delta}]_1[TiSe_2]_q$ compounds are given in Table 1. The

**Table 1. Lattice and Misfit Parameters for the $[(SnSe)_{1+\delta}]_1[TiSe_2]_q$ Heterostructures Determined from the X-ray Diffraction Patterns**

| $q$ | $[(SnSe)_{1+\delta}]$ $[TiSe_2]_q$ $c$-axis lattice parameter (nm) | SnSe $a$-axis lattice parameter (nm) | SnSe $b$-axis lattice parameter (nm) | $TiSe_2$ $a$-axis lattice parameter (nm) | $1 + \delta$ |
|---|---|---|---|---|---|
| 1 | 1.204(3) | 0.597(3) | 0.609(3) | 0.355(3) | 1.202(3) |
| 2 | 1.805(3) | 0.597(3) | 0.605(3) | 0.355(3) | 1.210(3) |
| 3 | 2.408(3) | 0.597(3) | 0.612(3) | 0.357(3) | 1.206(3) |
| 4 | 3.001(3) | 0.598(3) | 0.611(3) | 0.357(3) | 1.207(3) |
| 6 | 4.212(3) | 0.595(3) | 0.611(3) | 0.356(3) | 1.207(3) |
| 8 | 5.418(3) | 0.595(3) | 0.613(3) | 0.356(3) | 1.203(3) |
| 11 | 7.231(3) | 0.597(3) | 0.610(3) | 0.357(3) | 1.209(3) |
| 15 | 9.665(3) | 0.595(3) | 0.607(5) | 0.355(3) | 1.210(3) |

$c$-axis lattice parameter of $[(SnSe)_{1.2}]_1[TiSe_2]_1$ is 1.204(1) nm, which is in good agreement with that reported previously for the similar compounds.[24,31] The $c$-axis lattice parameter increases linearly as $q$ increases, with a slope of 0.602(1) nm per $TiSe_2$ layer. This thickness increase per $TiSe_2$ bilayer is consistent with the values reported for the $[(PbSe)_{1+\delta}]_1[TiSe_2]_q$ compounds.[51–53] The change per $TiSe_2$ layer is also consistent with the $c$-axis lattice parameter of 1T-$TiSe_2$ (0.6004 nm).[54] Extrapolating the $c$-axis lattice parameter to $q = 0$ yields an intercept of 0.600(8) nm, which corresponds to the thickness of the SnSe bilayer and the associated incommensurate interface thickness between the different structures. This thickness is larger than both the bulk SnSe $c$-axis lattice parameter of 0.5751(1) nm[55] and the change in the $c$-axis lattice parameter as the SnSe constituent is increased in thickness, while the $TSe_2$ thickness is kept constant in the $[(SnSe)_{1+\delta}]_q[TSe_2]_q$ (T = Ti, V, Nb, or Ta) heterostructures (0.5775–0.5806 nm).[24,32,56–58] The added thickness due to the interfaces on either side of SnSe is also similar to the difference between the extrapolated $TiSe_2$ trilayer thickness in the series $[(SnSe)_{1+\delta}]_m[TiSe_2]_1$ relative to the thickness of a $TiSe_2$ layer in 1T-$TiSe_2$.[24] The added thickness is probably due to the structural mismatch at the incommensurate interface between SnSe and $TiSe_2$.

Figure 3 contains in-plane diffraction patterns that were collected to provide information about the $a-b$-plane crystal structures of the two constituents. All reflections in these scans can be indexed as ($hk0$) reflections of either a hexagonal or a rectangular unit cell. The intensity of the rectangular unit cell decreases and that of the hexagonal cell increases as $q$ increases. This indicates that the rectangular unit cell is from the SnSe constituent and the hexagonal unit cell is from the $TiSe_2$ constituent. The position of the reflections remains approximately the same for all $q$ values, indicating that the in-plane structures of the two constituents do not change significantly with increasing $TiSe_2$ thickness.

The in-plane lattice parameters for each heterostructure are summarized in Table 1. The $a$-axis lattice parameter for the
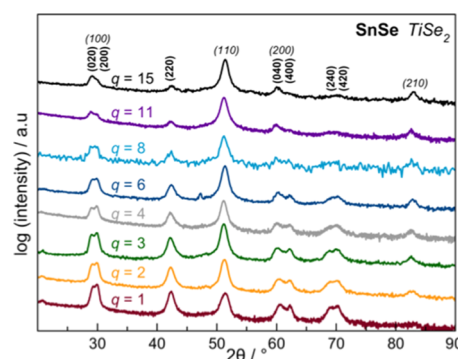


**Figure 3.** In-plane diffraction patterns of the $[(SnSe)_{1+\delta}][TiSe_2]_q$ heterostructures. All reflections can be indexed to ($hk0$) planes of either $TiSe_2$ or distorted SnSe, with the relative intensities of $TiSe_2$ reflections increasing with increasing $q$.

$TiSe_2$ constituent varies only slightly as $q$ is increased, with an average value of 0.356(1) nm. This agrees with the values previously reported for $TiSe_2$ in both $[(SnSe)_{1+\delta}]_1[TiSe_2]_1$ and $[(SnSe)_{1+\delta}]_m[TiSe_2]_1$,[23,24] as well as other $TiSe_2$-containing heterostructures.[59–64] Bulk $TiSe_2$ has an $a$-axis lattice parameter of 0.354 nm, which is within the error of the values found in Table 1. The SnSe rectangular basal plane unit cell does not change drastically as the thickness of the $TiSe_2$ constituent is increased. This is not surprising, as the SnSe layer has the same environment, with the $TiSe_2$ interfaces present on both sides of the single SnSe layer, in all of the heterostructures. The average lattice parameters for the SnSe basal plane summarized in Table 1 are 0.596(1) and 0.610(2) nm for the $a$-axis and $b$-axis lattice parameters, respectively. These are consistent with the values of 0.597(1) and 0.610(1) nm previously reported for the $[(SnSe)_{1+\delta}]_1[TiSe_2]_1$ heterostructure, but are larger than those in bulk SnSe.[23,24] The in-plane lattice parameters of SnSe can vary considerably in a heterostructure depending on the dichalcogenide with which it is layered.[65] The lattice parameters reflect the interactions between SnSe and the dichalcogenide, demonstrating the resulting tradeoffs in surface and volume free energy. The basal plane areas of SnSe and $TiSe_2$ remain relatively constant as $q$ is increased, resulting in an average misfit parameter $(1 + \delta)$ of 1.207(3) (Table 1). This misfit parameter is similar to what was previously reported for $[(SnSe)_{1+\delta}]_1[TiSe_2]_1$ and $[(SnSe)_{1+\delta}]_m[TiSe_2]_1$.[23,24,31]

HAADF-STEM was collected to provide local information about the heterostructures including layer stacking arrangement, constituent structures, extent of rotational disorder between constituent layers, and amount of disproportionation. Representative HAADF-STEM images of $[(SnSe)_{1+\delta}]_1[TiSe_2]_q$, with $q = 3$, 4, and 8, spanning the entire film thickness are shown in Figure 4. The two different constituent layers are distinguished by their $z$ contrast, with SnSe layers appearing brighter and $TiSe_2$ layers appearing darker. In the SnSe layers, the Sn atoms are brighter than the Se atoms. In all images, the targeted layering scheme is observed, indicating that the desired heterostructures were formed. Some damage from the focused ion beam sample preparation is visible, and the image for $q = 8$ has regions where the SnSe bilayer is missing. To further probe the global layering of the heterostructures, fast Fourier transforms (FFTs), Figure 4, were taken from the representative HAADF-STEM images. The expected Fourier components
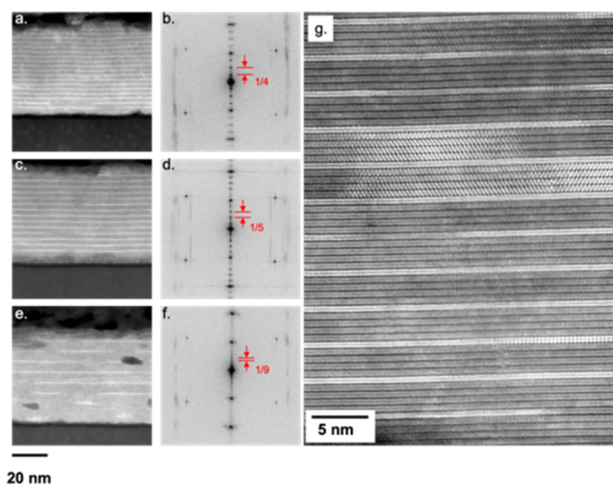
**Figure 4.** HAADF-STEM images and FFT's of the $[(SnSe)_{1+\delta}]_1[TiSe_2]_3$ (a, b), $[(SnSe)_{1+\delta}]_1[TiSe_2]_4$ (c, d), and $[(SnSe)_{1+\delta}]_1[TiSe_2]_8$ (e, f) and a higher-magnification HAADF-STEM image of a region of the $[(SnSe)_{1+\delta}]_1[TiSe_2]_4$ sample (g).

for each of the targeted compounds are observed, and the spacing between the Fourier components is consistent with the period measured in the specular diffraction pattern. The full-thickness HAADF-STEM images and their FFT indicate that the desired layering scheme makes up the majority of the films, which is consistent with the diffraction data discussed previously.

To probe the layer arrangement and zone axis stacking, a representative area from the $[(SnSe)_{1+\delta}]_1[TiSe_2]_4$ sample is

magnified and shown in Figure 4g. In this image, various zone axes and rotations off zone axes can be observed for both the constituent layers. This demonstrates the rotational disorder that occurs in the $a-b$-plane of the heterostructures. For both the SnSe and $TiSe_2$, layer regions can be located in the images aligned with (100) and (110) zones axes. These regions are not found in adjacent layers but are randomly distributed. Various layering defects are present in the film, but the majority of the area imaged is that of the targeted layering sequence. For example, the bottom SnSe layer in Figure 4g stops, while a $TiSe_2$ continues from that space. In the thicker block of $TiSe_2$, there are some unique stacking sequences where there is either twinning of the $TiSe_2$ layers or places where two different nucleation sites grew together. These layering defects and stacking sequences perhaps provide an opportunity to understand how the precursors self-assemble into the $[(SnSe)_{1+\delta}][TiSe_2]_q$ compounds; however, a more thorough investigation is required.

Room-temperature Seebeck coefficients collected from the $[(SnSe)_{1+\delta}]_1[TiSe_2]_q$ heterostructures (Figure 5a) are all negative, suggesting that electrons are the majority carrier. The magnitude of the Seebeck coefficient becomes systematically larger with increasing $q$, indicating that the carrier concentration decreases as the number of $TiSe_2$ layers is increased if we assume that the effective mass of the carriers does not change.[66,67] Koumoto suggested that charge carriers in $[SnSe]_1 TiSe_2$ result from the SnSe layer donating electrons to the $TiSe_2$ layer, which dominate the conduction.[16] If the amount of charge donated by the SnSe layer is constant, then the average electron concentration in the $TiSe_2$ layers would decrease as $q$ increases, which is consistent with the data and
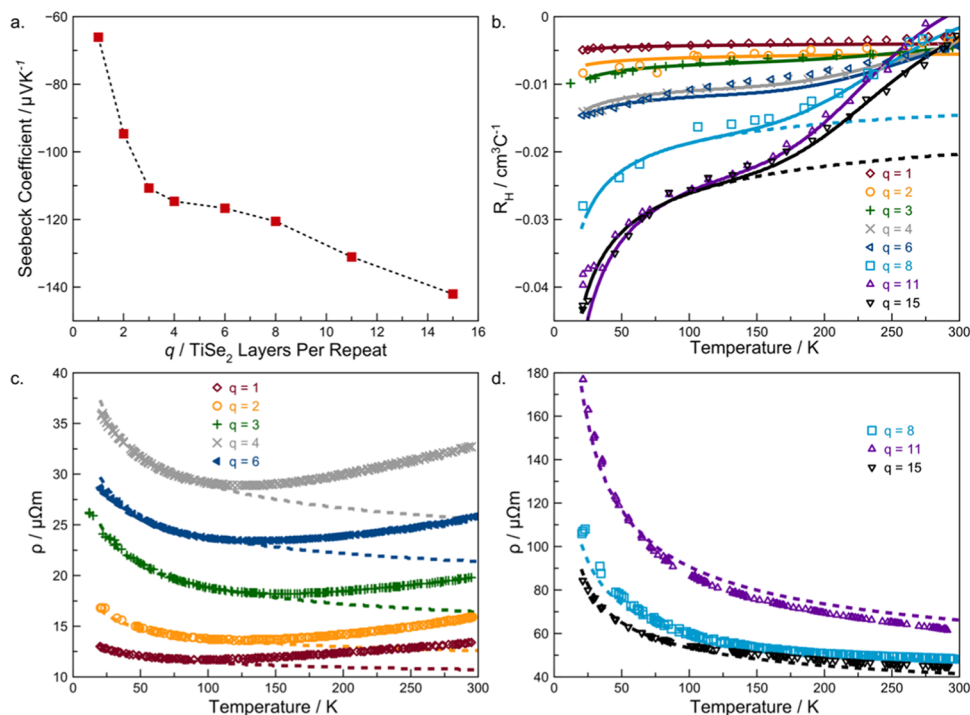


**Figure 5.** Seebeck coefficients for the $[(SnSe)_{1+\delta}]_1[TiSe_2]_q$ heterostructures plotted as a function of the number of $TiSe_2$ layers in the unit cell, $q$ (a). Temperature-dependent Hall coefficients (b) and resistivity data for the $[(SnSe)_{1+\delta}][TiSe_2]_q$ heterostructures. The resistivity data are plotted on two different resistivity scales ((c) $q = 1-6$ and (d) $q = 8-15$) so the temperature dependence in samples with thinner $TiSe_2$ layer blocks can be observed. The solid lines in (b) are models calculated from a two-carrier model with variable range hopping (VRH) at low temperatures as discussed in the text, which describes the entire temperature regime. The dashed lines in (b)−(d) show the fits to a VRH mechanism, which describes the Hall coefficient and resistivity at low temperatures.

prior reports of $(MX)_1(TiX_2)$ (M = Pb or Sn and X = S or Se) compounds.[52,53,66] The $q$-dependency of the Seebeck coefficient, however, has a much steeper negative slope for the $q \leq 3$ heterostructures than for $q \geq 3$ heterostructures, suggesting that there are two regimes dominated by different phenomena.

Variable temperature resistivity data collected from the $[(SnSe)_{1+\delta}]_1[TiSe_2]_q$ heterostructures are shown in Figure 5c,d. The temperature-dependent resistivity generally increases with more $TiSe_2$ layers present in the repeating unit (the $q = 6$ and 15 samples are exceptions). Samples $q = 6$ and 15 deviate from the trend, presumably due to different defect concentrations impacting carrier concentrations and/or mobility values. All samples have resistivity upturns as the temperature is lowered, with the temperature where the upturn begins increasing as $q$ gets larger. For samples with the largest number of $TiSe_2$ layers in the repeating unit, the resistivity continually goes up with decreasing temperature over the entire temperature regime. The samples with smaller $q$ have a decrease in the resistivity with decreasing temperature from room temperature. Below a certain sample-dependent temperature, the resistivity increases as the temperature is decreased. The initial decrease in the resistivity for the $q = 1-4$ and 6 heterostructures is consistent with the decreased electron–phonon scattering with the lowering of temperature, as expected for a metal. Overall, the rate of resistivity increase at low temperatures for all of the samples is not as large as would be expected for semiconducting behavior. For samples with more $TiSe_2$ layers in the repeating unit, the upturn in the temperature-dependent resistivity is similar to previous reports on $TiSe_2$ where the samples were reported to have low defect concentrations.[20]

To further probe the transport behavior, Hall coefficients were measured for the $[(SnSe)_{1+\delta}]_1[TiSe_2]_q$ heterostructures as a function of temperature (Figure 5b). Each heterostructure exhibits a negative Hall coefficient throughout the entire temperature range, which is consistent with the negative room-temperature Seebeck coefficients (Figure 5a). However, it appears as if the samples with $q \geq 8$ will have positive Hall coefficients at temperatures slightly above the range measured (above ~300 K). At low temperatures, the negative Hall coefficient with decreasing temperature suggests that electrons dominate the transport properties in this regime. The increase in the magnitude of the Hall coefficient with decreasing temperature, which systematically increases as $q$ gets larger, implies that the carrier concentration decreases as the temperature is decreased and decreases more in high $q$ heterostructures. The temperature dependence of the samples with larger $q$ values also suggests that there are two different phenomena present, one that dominates at low temperatures and one that dominates at high temperatures.

The transport properties of all samples in the low-temperature regime suggest that the carrier concentration decreases as temperature declines. As $q$, the number of $TiSe_2$ layers in the repeating unit gets bigger, both the upturns in resistivity and the systematic increase in the absolute magnitude of the Hall coefficient get larger. The temperature dependence of the resistivity at low temperatures cannot be fit to an exponential for any of the samples (see Figure S1). This suggests that the decrease in the resistivity as the temperature is increased does not result from excitation across a band gap. A charge or spin density wave would be consistent with a decrease in carriers as the temperature is lowered; however, we

did not find any discontinuities in lattice parameters as a function of temperature (see Figure S2). Similar nonexponential temperature dependence in the resistivity and Hall coefficient data has been observed in other materials and attributed to variable range hopping (VRH). VRH is commonly observed in disordered systems and is identified by its characteristic ln resistivity vs $T^{-1/4}$ temperature dependency.[68–73]

The low-temperature transport data from all heterostructures was fit with a VRH model assuming a single-band approximation at low temperatures. The resistivity data was fit to the following equation

$$\rho(T) = \rho_o \exp[(T_M/T)^{1/4}] \tag{1}$$

where $\rho(T)$ is the resistivity as a function of temperature, $\rho_o$ is the resistivity when all of the carriers are mobile, $T$ is the temperature, and $T_M$ is the characteristic temperature related to the energy needed for hopping to occur.[71] The temperature dependence of the Hall coefficients was fit to the following equation

$$R_H = \frac{-1}{|e|n(T)} = -\left( \frac{\exp\left[\left(\frac{T_M}{T}\right)^{1/4}\right]}{|e|n_0} \right) \tag{2}$$

where $n(T)$ is the number of mobile carriers and $n_o$ is the total number of carriers that can become mobile. $n_o = 1/\rho_o e\mu$ where $\mu$ is the mobility. These equations fit the transport data below 150 K for all values of $q$ well (Figure 5b–d).

As shown in Figure 6, the fitted $n_o$ values generally decrease as the number of $TiSe_2$ layers in the unit cell increases. The
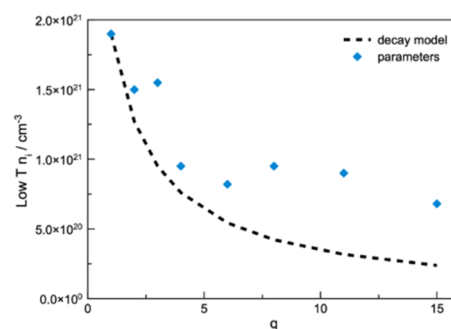


**Figure 6.** Values of the number of carriers that can become mobile for the low-temperature-activated process, $n_o$, plotted as a function of the number of $TiSe_2$ layers in the sample. $n_o$ values were obtained by fitting the low-temperature transport data using a single-band, variable range hopping model. The dashed line assumes that $n_o$ should vary as $n_{SnSe \rightarrow TiSe_2}/q + 1$, where $q$ is the number of the $TiSe_2$ layers in the heterostructures, and use the $n_{SnSe \rightarrow TiSe_2}$ obtained from the $[(SnSe)_{1+\delta}]_1[TiSe_2]_1$ compound.

carriers donated by SnSe to adjacent $TiSe_2$ layers ($n_{SnSe \rightarrow TiSe_2}$) are diluted by additional $TiSe_2$ layers as $q$ increases. If the amount of charge donated is constant in this family of compounds, an estimate for $n_{SnSe \rightarrow TiSe_2}$ would be the value of $n_o$ in the $[(SnSe)_{1+\delta}]_1[TiSe_2]_1$ compound. This value is consistent with the previous estimates of the amount of charge donated from the SnSe or PbSe layers to $TiSe_2$ layers.[52,53,66] The amount of charge donated is about 1/10 of an electron per

**Table 2. Parameters Obtained for Fits of the Temperature-Dependent Hall Coefficient and Resistivity Transport Data[a]**

| | $\mu_h$ (cm$^2$ V$^{-1}$ s$^{-1}$) | $\mu_e$ (cm$^2$ V$^{-1}$ s$^{-1}$) | | $n_i$ (cm$^{-3}$) | | | |
|---|---|---|---|---|---|---|---|
| $q$ | high $T$ | high $T$ | low $T$ | high $T$ | low $T$ | $E_a$ (meV) | $T_m$ (K) |
| 1 | NA | NA | 3.75 | NA | $1.9 \times 10^{21}$ | NA | 0.5 |
| 2 | NA | NA | 4.4 | NA | $1.5 \times 10^{21}$ | NA | 2 |
| 3 | 5 | 1 | 3.8 | $3.70 \times 10^{21}$ | $1.55 \times 10^{21}$ | 110 | 11 |
| 4 | 6 | 1 | 3.8 | $5.92 \times 10^{21}$ | $9.5 \times 10^{20}$ | 107 | 7 |
| 6 | 6.5 | 1 | 5.0 | $8.46 \times 10^{21}$ | $8.2 \times 10^{20}$ | 107 | 4 |
| 8 | 5 | 1 | 3.1 | $9.87 \times 10^{21}$ | $9.5 \times 10^{20}$ | 113 | 120 |
| 11 | 5.5 | 1 | 2.85 | $1.11 \times 10^{22}$ | $9.0 \times 10^{20}$ | 115 | 300 |
| 15 | 5.4 | 1 | 4.9 | $1.20 \times 10^{22}$ | $6.8 \times 10^{20}$ | 113 | 120 |

[a]Parameters we determined assuming charge transfer from SnSe to TiSe$_2$ result in carriers that are localized at low temperature due to variable range hopping, and at high temperatures, holes and additional electrons are created due to activation of carriers across a band gap requiring a two-carrier model. The low-temperature parameters were used to fit the VRH model and the two-carrier model with VRH at low temperatures.

SnSe bilayer, which suggests that there is a significant electrostatic interaction between the constituent layers that helps to stabilize these compounds. $n_o$ would vary as $n_{SnSe \rightarrow TiSe_2}/q + 1$, where $q$ is the number of TiSe$_2$ layers in the heterostructures if the amount of charge donated was constant. The calculated values from this simple model consistently underestimate the $n_o$ values derived from the fits to the data, suggesting that the amount of charge donation increases as $q$ increases (see Figure 6). Defects in the TiSe$_2$ layers also become an increasingly important source of potential carriers as $q$ increases. The values of $T_M$ obtained from the fits increase systematically as $q$ increases (see Table 2). The increase in the $T_M$ values correlates with a decrease in the average carrier concentration, suggesting that decreased screening causes an increase in localization. Edwards and Sienko correlated the behavior of many systems that undergo a metal to nonmetal transition,[74] showing that carriers become localized when the product of the carrier concentration and the effective Bohr radius reach a critical value. The behavior observed here suggests that a metal to nonmetal transition is occurring, in part driven by disorder, as carrier concentration is decreased. Further analysis looking at the derivatives of conductivity has been proposed by Möbius to determine the origin of the metal to nonmetal transition, but requires careful temperature equilibration before the transport properties are measured.[75]

Mobility values were calculated directly from the resistivity and Hall data at low temperatures where electrons dominate the transport behavior. The average mobility values in the low-temperature regime are given in Table 2. The values range from 2.85 to 5.0 cm$^2$ V$^{-1}$ s$^{-1}$ with an average value of 4.0(8) cm$^2$ V$^{-1}$ s$^{-1}$ and do not systematically change as the number of TiSe$_2$ layers is varied. These mobility values are similar to those reported previously for the $[(SnSe)_{1+\delta}]_m[TiSe_2]_q$ misfit layer compounds and low compared to the values previously reported for bulk and thin-film TiSe$_2$.[26,31,76]

The Hall coefficient data above 150 K for samples with a large number of TiSe$_2$ layers in the repeating unit cell suggests that there is another process that results in the activation of additional carriers. Recently, Watson et al. suggested that the electrical properties of TiSe$_2$ are dominated by either electrons or holes depending on the temperature regime. At low temperatures, the transport behavior of TiSe$_2$ is dominated by electrons from defects, but above 150 K, activation of intrinsic carriers occurs and holes become increasingly important in the transport. The influence of the activated holes becomes more pronounced due to their higher mobility relative to their

electron counterparts.[77] We fit our transport data to the two-carrier model suggested by Watson et al., with an additional term for the electrons donated from SnSe to the TiSe$_2$ layers at low temperature

$$R_H = \frac{[\mu_h^2 n_h - \mu_{e(high\ T)}^2 n_{e(high\ T)} - \mu_{e(low\ T)}^2 n_{e(low\ T)}}{\{|e|[\mu_h n_h + \mu_{e(high\ T)} n_{e(high\ T)} + \mu_{e(low\ T)} n_{e(low\ T)}]^2\}} \quad (3)$$

In eq 3 $\mu_h$, $\mu_{e(high\ T)}$, and $\mu_{e(low\ T)}$ are the hole and electron mobilities and $n_h$, $n_{e(low\ T)}$, and $n_{e(low\ T)}$ are the hole and electron carrier concentrations, respectively.[77] The mobility values were assumed to be temperature independent. This model is not sensitive to the mobility of the electrons created from the high-temperature process because the larger number of electrons from the low-temperature process dominates the average electron mobility. We assumed that the mobility values for the holes dominate the high-temperature process due to their higher mobility, as suggested by Watson, and set $\mu_{e(low\ T)}$ = 1 cm$^2$ V$^{-1}$ s$^{-1}$. The hole concentration was assumed to come only from activation at high temperatures (eq 4)

$$n_h = n_{i(highT)}\ e^{[-Ea/kT]} \quad (4)$$

The electron concentration was assumed to be the sum of the low- and high-temperature carriers (eq 5)

$$n_e = n_{e(lowT)} + n_{e(highT)} \quad (5)$$

where

$$n_{e(lowT)} = n_{i(lowT)}/\exp[(T/T_M)^{1/4}] \quad (6)$$

$$n_{e(highT)} = n_{i(highT)}\ e^{[-Ea/kT]} \quad (7)$$

The fits are not very sensitive to the value of $n_{i(high\ T)}$ due to the small temperature range, for which there is data. We set $n_{i(high\ T)}$ to be close to the density of Se atoms in TiSe$_2$ ($n_{TiSe_2}$). Since charge transfer between SnSe and TiSe$_2$ will modify the electronic structure of layers close to the interface, the fraction of bulk-like TiSe$_2$ in each unit cell varies as

$$[(q - x)/(q + 1)] \quad (8)$$

where $q$ is the number of TiSe$_2$ layers in the unit cell, $q + 1$ is the total number of layers (SnSe + TiSe$_2$) in the unit cell, and $x$ is the number of layers near the interface that do not behave as bulk TiSe$_2$ due to the charge transfer. Therefore,

$$n_{i(highT)} = n_{TiSe_2}[(q - x)/(q + 1)] \quad (9)$$

The high-temperature carrier concentration, $n_{i(high\ T)}$, calculated with $x = 2$ gave the most constant values for the hole mobilities and high-temperature activation energy ($E_a$) across all samples. This is reasonable since there are two TiSe$_2$ layers adjacent to SnSe, which will be most impacted by the charge donated by SnSe to TiSe$_2$.

The model does reasonably well at fitting the temperature dependence of the Hall coefficients, with the solid lines in Figure 5b demonstrating the result of the fits for each sample. The low-temperature fitted values for the low-temperature $T_M$ (Table 2) and the low-temperature carrier concentration ($n_{i(low\ T)}$) (Figure 6) were used in these fits. The values for the hole mobilities and high-temperature activation energy ($E_a$) are similar for all of the samples. The average activation energy for the high-temperature carriers, ~0.11(1) eV, is similar to the values previously reported for bulk TiSe$_2$.[78] The average hole mobility value, $\mu_h$, is 5.4(1) cm$^2$ V$^{-1}$ s$^{-1}$, which is higher than the values previously reported for the $[(SnSe)_{1+\delta}]_m[TiSe_2]_q$ misfit layer compounds[31] and lower than the range reported previously for TiSe$_2$.[26,76] The hole mobility needs to be higher than the mobility of the electrons created by excitation across the gap to reproduce the decreasing absolute value of the Hall coefficient observed as temperature increases.[77]

The resistivity is given by the following equation

$$\rho \frac{1}{\sigma} = \frac{1}{[|e|(\mu_h n_h + \mu_{e(high\ T)} n_{e(high\ T)} + \mu_{e(low\ T)} n_{e(low\ T)})]} \quad (10)$$

where $\mu_h$, $n_h$, $\mu_e$, and $n_e$ are defined as described above. The values obtained for the carrier concentration, mobility, activation energy, and characteristic hopping energy from fitting the Hall coefficient data to the two-carrier model (Table 2) reproduce the low-temperature resistivity data reasonable for all of the samples (Figure 5). This suggests that the resistivity can be described by a single carrier model in this temperature range. The agreement at high temperature is not good, as the model underestimates the resistivity. This suggests that the assumption of a temperature-independent mobility is not valid.

DFT was used to model the electronic structure of bulk SnSe, TiSe$_2$, the surfaces of each, and a large-scale epitaxial model of the $q = 1$ system to further understand the properties observed in the heterostructures. Following the computational procedure detailed in the Methods and Materials section, three key properties were obtained: (i) the electronic band gaps of both bulk materials, (ii) the work functions for slab models thereof, and (iii) representative charge densities in both the slab and epitaxial models. Together, these properties provide additional and complementary insights into the mechanism of charge donation in the $[(SnSe)_{1+\delta}]_1[TiSe_2]_q$ heterostructures. The electronic band gaps of bulk SnSe and TiSe$_2$ were computed using the hybrid generalized gradient approximation (GGA) functional, HSE06,[79] known to perform well for narrow-gap semiconductors. As informed by the crystallography, SnSe is modeled as face-centered cubic, whose band gap is predicted to be 0.5 eV. Other crystal polymorphs were also explored, and their band gaps are presented in Table S1, Supporting Information. The work function ($\Phi = 4.3$ eV) was recovered using a surface slab model and permits the alignment of the valence band energy, and therefore computational Fermi level, to the vacuum (Figure 7). A seven-layer slab was used to sufficiently account for the bulk, as well as its
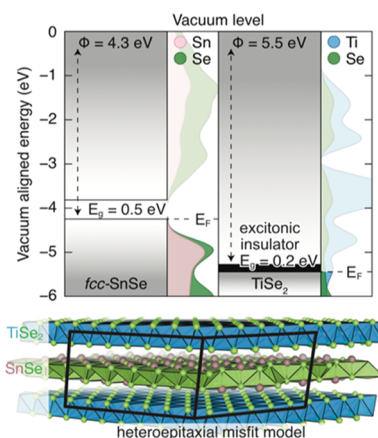


**Figure 7.** Vacuum-aligned density of states for SnSe and TiSe$_2$ slab models. The frontier valence of SnSe is ~1.2 eV above that of TiSe$_2$, indicating that charge transfer from SnSe to TiSe$_2$ would occur at the interface between them.

surface, and was aligned using a method previously described.[44] A similar procedure was performed for TiSe$_2$; however, both GGA and hybrid GGA approaches are known to predict bulk metallicity in TiSe$_2$,[80,81] despite experimental evidence for a thermally activated transport mechanism. Indeed, a narrow band gap (200−300 meV) is recovered using a GW approach,[82] but the procedure does not significantly augment the work function. Here, the nature of the gap is less important than the work function. Hence, TiSe$_2$ is presented as a bulk metal with a work function of 5.5 eV (Figure 7). A comparison of these computed work functions suggests that spontaneous charge transfer should occur between SnSe and TiSe$_2$, as the valence band of the former lays above the conduction band of the latter.

To test this hypothesis, a lattice-matched $[(SnSe)_{1+\delta}]_1[TiSe_2]_1$ model was constructed, minimizing the lattice mismatch by expanding the unit in the $a−b$ plane to a 6 × 7 supercell, as shown in Figure 7. A Bader charge analysis[47] was done on bulk SnSe and TiSe$_2$ and the lattice-matched $[(SnSe)_{1+\delta}]_1[TiSe_2]_1$ to provide a quantitative estimate of the extent of charge transfer between the materials.

In the bulk structures, positive charges are observed on the cations and negative charges are observed on the anions. The smaller negative charge on the Se in TiSe$_2$ reflects the covalent hybridization of the Ti and Se orbitals in this compound. By comparing the charges in the bulk structures with the charges calculated for the lattice-matched heterostructure, a charge transfer from SnSe to TiSe$_2$ is observed in the heterostructure (Table 3). The magnitude of the electron transfer from SnSe to TiSe$_2$ is approximately 10%, in excellent agreement with the

**Table 3. Average Atomic Charge of Bulk SnSe, Bulk TiSe$_2$, and the Average Charge Transfer between Them in the Heterojunction**

| | avg charge in bulk (b$^{-3}$) | avg charge in heterostructure (b$^{-3}$) | avg charge transfer (b$^{-3}$) |
|---|---|---|---|
| Sn | 0.777 | 0.860 | 0.083 |
| Ti | 1.341 | 1.345 | 0.004 |
| Se in SnSe | −0.777 | −0.729 | 0.048 |
| Se in TiSe$_2$ | −0.671 | −0.747 | −0.076 |

experimental observation of 1/10th of an electron per formula unit. Interestingly, the added charge in $TiSe_2$ is localized on the Se rather than the Ti, reflecting the extent of covalent character in the bonding of this compound. There is a net "ionic" bond between the layers of SnSe and $TiSe_2$, with higher electron density in the lone pair of the Se atoms in $TiSe_2$ and a positive charge in the SnSe planes. This picture agrees well with the analysis of the transport properties, which suggests that the two $TiSe_2$ layers adjacent to SnSe have different transport properties than those not adjacent to SnSe. The added charge to the conduction band indicated in the calculation agrees well with the metallic-like conductivities observed for the small $q$ heterostructures above the hopping temperature. The calculation also provides a basis for the model shown in Figure 7. A calculation of the stabilization energy of the ionic "bond" between the layers is surprisingly high, 3.6 eV, suggesting that this interaction is a key factor in stabilizing the heterostructures. This ionic interaction between the layers makes $[(SnSe)_{1+\delta}]_1[TiSe_2]_1$ more stable than a physical mixture of SnSe and $TiSe_2$ by ~0.09 eV, consistent with the thermodynamic stability of the known misfit layer compound.[15]

## CONCLUSIONS

A series of compounds $[(SnSe)_{1+\delta}]_1[TiSe_2]_q$ were prepared, and the structural data indicates that the structures of the constituent layers are similar in all of the heterostructures. The electrical properties suggest that charge donation from the SnSe to the $TiSe_2$ layers occurs, resulting in metallic behavior for samples with a low number of $TiSe_2$ layers. The carrier concentration decreases as the number of $TiSe_2$ layers increases. Localization of the carriers occurs at low temperature, with the temperature required to activate the hopping of these carriers increasing as the $TiSe_2$ layer thickness is increased. DFT calculations show that the valence band of SnSe is higher in energy than the conduction band of $TiSe_2$, supporting the experimentally suggested charge transfer from SnSe to $TiSe_2$. The calculations suggest that the charge transfer between the constituents contributes a significant "ionic" stabilization of these heterostructures, which may be the key factor in their kinetic stability. Similar charge-transfer effects will be present in all heterostructures to equalize the chemical potential, and understanding how they modify properties is necessary for the synthesis of novel materials with the designer properties.

## ASSOCIATED CONTENT

### Ⓢ Supporting Information

The Supporting Information is available free of charge at https://pubs.acs.org/doi/10.1021/acs.chemmater.0c01691.

> X-ray reflectivity patterns of representative heterostructures before and after annealing at 350 °C for 30 min in a $N_2$ atmosphere, very low-temperature-dependent resistivity measurements of representative heterostructures, demonstrating the nonexponential behavior with decreasing temperature, temperature-dependent in-plane lattice parameters of both constituents, demonstrating that the structures do not change as temperature decreases, and DFT-calculated electronic band gaps (PDF)

> Crystallographic information file containing the PBEsol-optimized computational structure of the SnSe seven-layer slab (CIF)
> Crystallographic information file containing the PBEsol-optimized computational structure of the SnSe monolayer (CIF)
> Crystallographic information file containing the PBEsol-optimized computational structure of the SnSe−$TiSe_2$ one layer to one layer heterojunction (CIF)
> Crystallographic information file containing the PBEsol-optimized computational structure of the $TiSe_2$ seven-layer slab (CIF)
> Crystallographic information file containing the PBEsol-optimized computational structure of the $TiSe_2$ monolayer (CIF)

## AUTHOR INFORMATION

### Corresponding Author

**David C. Johnson** − *Department of Chemistry and Materials Science Institute, University of Oregon, Eugene, Oregon 97403, United States;* ⓘ orcid.org/0000-0002-1118-0997; Email: davej@uoregon.edu

### Authors

**Danielle M. Hamann** − *Department of Chemistry and Materials Science Institute, University of Oregon, Eugene, Oregon 97403, United States;* ⓘ orcid.org/0000-0002-9262-1060

**Dylan Bardgett** − *Department of Chemistry and Materials Science Institute, University of Oregon, Eugene, Oregon 97403, United States*

**Sage R. Bauers** − *Department of Chemistry and Materials Science Institute, University of Oregon, Eugene, Oregon 97403, United States*

**Thomas W. Kasel** − *Department of Chemistry and Materials Science Institute, University of Oregon, Eugene, Oregon 97403, United States*

**Austin M. Mroz** − *Department of Chemistry and Materials Science Institute, University of Oregon, Eugene, Oregon 97403, United States;* ⓘ orcid.org/0000-0003-4166-8093

**Christopher H. Hendon** − *Department of Chemistry and Materials Science Institute, University of Oregon, Eugene, Oregon 97403, United States;* ⓘ orcid.org/0000-0002-7132-768X

**Douglas L. Medlin** − *Sandia National Laboratories, Livermore, California 94551, United States*

Complete contact information is available at:
https://pubs.acs.org/10.1021/acs.chemmater.0c01691

### Author Contributions

The manuscript was written through the contributions of all authors.

### Notes

The authors declare no competing financial interest.

## ◼ ABBREVIATIONS

2D, two-dimensional; DFT, density functional theory; XRD, X-ray diffraction; XRR, X-ray reflectivity; FIB-SEM, focused ion beam scanning electron microscope; HAADF-STEM, high-angle annular dark-field scanning transmission electron microscopy; VASP, Vienna Ab initio Simulation; PAW, projector-augmented wave; VRH, variable range hopping

## ◼ REFERENCES

(1) Ni, Z. H.; Wang, H. M.; Kasim, J.; Fan, H. M.; Yu, T.; Wu, Y. H.; Feng, Y. P.; Shen, Z. X. Graphene Thickness Determination Using Reflection and Contrast Spectroscopy. *Nano Lett.* **2007**, *7*, 2758−2763.

(2) Mak, K. F.; Lee, C.; Hone, J.; Shan, J.; Heinz, T. F. Atomically Thin $MoS_2$: A New Direct-Gap Semiconductor. *Phys. Rev. Lett.* **2010**, *105*, No. 136805.

(3) Tongay, S.; Zhou, J.; Ataca, C.; Lo, K.; Matthews, T. S.; Li, J.; Grossman, J. C.; Wu, J. Thermally Driven Crossover from Indirect toward Direct Bandgap in 2D Semiconductors: $MoSe_2$ versus $MoS_2$. *Nano Lett.* **2012**, *12*, 5576−5580.

(4) Bolotin, K. I.; Ghahari, F.; Shulman, M. D.; Stormer, H. L.; Kim, P. Observation of the Fractional Quantum Hall Effect in Graphene. *Nature* **2009**, *462*, 196−199.

(5) Dean, C. R.; Wang, L.; Maher, P.; Forsythe, C.; Ghahari, F.; Gao, Y.; Katoch, J.; Ishigami, M.; Moon, P.; Koshino, M.; et al. Hofstadter's Butterfly and the Fractal Quantum Hall Effect in Moiré Superlattices. *Nature* **2013**, *497*, 598−602.

(6) Ponomarenko, L. A.; Gorbachev, R. V.; Yu, G. L.; Elias, D. C.; Jalil, R.; Patel, A. A.; Mishchenko, A.; Mayorov, A. S.; Woods, C. R.; Wallbank, J. R.; et al. Cloning of Dirac Fermions in Graphene Superlattices. *Nature* **2013**, *497*, 594−597.

(7) Hunt, B.; Sanchez-Yamagishi, J. D.; Young, A. F.; Yankowitz, M.; LeRoy, B. J.; Watanabe, K.; Taniguchi, T.; Moon, P.; Koshino, M.; Jarillo-Herrero, P.; et al. Massive Dirac Fermions and Hofstadter Butterfly in a van Der Waals Heterostructure. *Science* **2013**, *340*, 1427−1430.

(8) Schaibley, J. R.; Yu, H.; Clark, G.; Rivera, P.; Ross, J. S.; Seyler, K. L.; Yao, W.; Xu, X. Valleytronics in 2D Materials. *Nat. Rev. Mater.* **2016**, *1*, No. 16055.

(9) Geim, A. K.; Grigorieva, I. V. Van Der Waals Heterostructures. *Nature* **2013**, *499*, 419−425.

(10) Novoselov, K. S.; Mishchenko, A.; Carvalho, A.; Castro Neto, A. H. 2D Materials and van Der Waals Heterostructures. *Science.* **2016**, *353*, No. aac9439.

(11) Jariwala, D.; Sangwan, V. K.; Lauhon, L. J.; Marks, T. J.; Hersam, M. C. Emerging Device Applications for Semiconducting Two-Dimensional Transition Metal Dichalcogenides. *ACS Nano* **2014**, *8*, 1102−1120.

(12) Cui, X.; Lee, G. H.; Kim, Y. D.; Arefe, G.; Huang, P. Y.; Lee, C. H.; Chenet, D. A.; Zhang, X.; Wang, L.; Ye, F.; et al. Multi-Terminal Transport Measurements of $MoS_2$ Using a van Der Waals Heterostructure Device Platform. *Nat. Nanotechnol.* **2015**, *10*, 534−540.

(13) Grubišić Čabo, A.; Miwa, J. A.; Grønborg, S. S.; Riley, J. M.; Johannsen, J. C.; Cacho, C.; Alexander, O.; Chapman, R. T.; Springate, E.; Grioni, M.; et al. Observation of Ultrafast Free Carrier Dynamics in Single Layer $MoS_2$. *Nano Lett.* **2015**, *15*, 5883−5887.

(14) Wang, Y. Y.; Ni, Z. H.; Yu, T.; Shen, Z. X.; Wang, H. M.; Wu, Y. H.; Chen, W.; Wee, A. T. S. Raman Studies of Monolayer Graphene: The Substrate Effect. *J. Phys. Chem. C* **2008**, *112*, 10637−10640.

(15) Song, Y. J.; Kim, M. J.; Jung, W. G.; Kim, B.-J.; Rhyee, J.-S. Superconducting Properties of the Misfit-Layer Compound $(SnSe)_{1.18}(TiSe_2)_2$. *Phys. Status Solidi B* **2016**, *253*, 1517−1522.

(16) Wan, C.; Wang, Y.; Wang, N.; Koumoto, K. Low-Thermal-Conductivity $(MS)_{1+x}(TiS_2)_2$ (M = Pb, Bi, Sn) Misfit Layer Compounds for Bulk Thermoelectric Materials. *Materials* **2010**, *3*, 2606−2617.

(17) Ryu, Y. K.; Frisenda, R.; Castellanos-Gomez, A. Superlattices Based on van Der Waals 2D Materials. *Chem. Commun.* **2019**, *55*, 11498−11510.

(18) Radovsky, G.; Popovitz-Biro, R.; Stroppa, D. G.; Houben, L.; Tenne, R. Nanotubes from Chalcogenide Misfit Compounds: Sn-S and Nb-Pb-S. *Acc. Chem. Res.* **2014**, *47*, 406−416.

(19) Meerschaut, A. Misfit Layer Compounds Abbreviations CT DOS REELS XAS XPS VdW Charge Transfer Density of States Reflection Electron Energy Loss Spectroscopy X-Ray Absorption Spectroscopy X-ray Photoelectron Spectroscopy van Der Waals. *Curr. Opin. Solid State Mater. Sci.* **1996**, *1*, 250−260.

(20) Huang, S. H.; Shu, G. J.; Pai, W. W.; Liu, H. L.; Chou, F. C. Tunable Se Vacancy Defects and the Unconventional Charge Density Wave in $1T\text{-}TiSe_{2-\delta}$. *Phys. Rev. B* **2017**, *95*, No. 045310.

(21) Levy, F. Electrical Resistivity and Hall Effect in $TiSe_2$ Containing Vanadium Impurities. *J. Phys. C: Solid State Phys.* **1979**, *12*, 3725−3732.

(22) Levy, F. The Influence of Impurities on the Electrical Properties of $TiSe_2$ Single Crystals. *J. Phys. C: Solid State Phys.* **1980**, *13*, 2901−2912.

(23) Hamann, D. M.; Merrill, D. R.; Bauers, S. R.; Mitchson, G.; Ditto, J.; Rudin, S. P.; Johnson, D. C. Long-Range Order in $[(SnSe)_{1.2}]_1[TiSe_2]_1$ Prepared from Designed Precursors. *Inorg. Chem.* **2017**, *56*, 3499−3505.

(24) Hamann, D. M.; Lygo, A. C.; Esters, M.; Merrill, D. R.; Ditto, J.; Sutherland, D. R.; Bauers, S. R.; Johnson, D. C. Structural Changes as a Function of Thickness in $[(SnSe)_{1+\delta}]_m TiSe_2$ Heterostructures. *ACS Nano* **2018**, *12*, 1285−1295.

(25) Rasch, J.; Stemmler, T.; Müller, B.; Dudy, L.; Manzke, R. 1T-$TiSe_2$: Semimetal or Semiconductor? *Phys. Rev. Lett.* **2008**, No. 237602.

(26) Di Salvo, F. J.; Moncton, D. E.; Waszczak, J. V. Electronic Properties and Superlattice Formation in the Semimetal $TiSe_2$. *Phys. Rev. B* **1976**, *14*, 4321−4328.

(27) Fang, C. M.; De Groot, R. A.; Haas, C. Bulk and Surface Electronic Structure of $1T\text{-}TiS_2$ and $1T\text{-}TiSe_2$. *Phys. Rev. B* **1997**, 4455.

(28) Zhao, L. D.; Lo, S. H.; Zhang, Y.; Sun, H.; Tan, G.; Uher, C.; Wolverton, C.; Dravid, V. P.; Kanatzidis, M. G. Ultralow Thermal Conductivity and High Thermoelectric Figure of Merit in SnSe Crystals. *Nature* **2014**, *508*, 373−377.

(29) Jin, W.; Vishwanath, S.; Liu, J.; Kong, L.; Lou, R.; Dai, Z.; Sadowski, J. T.; Liu, X.; Lien, H. H.; Chaney, A.; et al. Electronic Structure of the Metastable Epitaxial Rock-Salt SnSe {111} Topological Crystalline Insulator. *Phys. Rev. X* **2017**, *7*, No. 041020.

(30) Cui, Z.; Wang, X.; Ding, Y.; Li, M. Exploration Work Function and Optical Properties of Monolayer SnSe Allotropes. *Superlattices Microstruct.* **2018**, *114*, 251−258.

(31) Merrill, D. R.; Moore, D. B.; Ditto, J.; Sutherland, D. R.; Falmbigl, M.; Winkler, M.; Pernau, H.-F.; Johnson, D. C. The Synthesis, Structure, and Electrical Characterization of $(SnSe)_{1.2}TiSe_2$. *Eur. J. Inorg. Chem.* **2015**, *2015*, 83−91.

(32) Atkins, R.; Wilson, J.; Zschack, P.; Grosse, C.; Neumann, W.; Johnson, D. C. Synthesis of $[(SnSe)_{1.15}]m((TaSe_2)_n$ Ferecrystals: Structurally Tunable Metallic Compounds. *Chem. Mater.* **2012**, *24*, 4594−4599.

(33) Johnson, D. C. Controlled Synthesis of New Compounds Using Modulated Elemental Reactants. *Curr. Opin. Solid State Mater. Sci.* **1998**, *3*, 159−167.

(34) Esters, M. *Deposition Software for the Inficon IC6 Deposition Controller*; GitHub, 2017. https://github.com/marcoesters/deposition_ic6 (accessed Nov 8, 2017).

(35) Jain, A.; Ong, S. P.; Hautier, G.; Chen, W.; Richards, W. D.; Dacek, S.; Cholia, S.; Gunter, D.; Skinner, D.; Ceder, G.; et al. Commentary: The Materials Project: A Materials Genome Approach to Accelerating Materials Innovation. *APL Mater.* **2013**, *1*, No. 011002.

(36) Perdew, J. P.; Burke, K.; Ernzerhof, M. Generalized Gradient Approximation Made Simple. *Phys. Rev. Lett.* **1996**, *77*, 3865−3868.

(37) Perdew, J. P.; Ruzsinszky, A.; Csonka, G. I.; Vydrov, O. A.; Scuseria, G. E.; Constantin, L. A.; Zhou, X.; Burke, K. Restoring the Density-Gradient Expansion for Exchange in Solids and Surfaces. *Phys. Rev. Lett.* **2008**, *100*, No. 136406.

(38) Tkatchenko, A.; Scheffler, M. Accurate Molecular Van Der Waals Interactions from Ground-State Electron Density and Free-Atom Reference Data. *Phys. Rev. Lett.* **2009**, *102*, No. 073005.

(39) Blöchl, P. E. Projector Augmented-Wave Method. *Phys. Rev. B* **1994**, *50*, 17953−17979.

(40) Kresse, G.; Hafner, J. Ab Initio Molecular-Dynamics Simulation of the Liquid-Metal−Amorphous-Semiconductor Transition in Germanium. *Phys. Rev. B* **1994**, *49*, 14251−14269.

(41) Kresse, G.; Furthmüller, J. Efficient Iterative Schemes for Ab Initio Total-Energy Calculations Using a Plane-Wave Basis Set. *Phys. Rev. B: Condens. Matter Mater. Phys.* **1996**, *54*, 11169−11186.

(42) Kresse, G.; Furthmüller, J. Efficiency of Ab-Initio Total Energy Calculations for Metals and Semiconductors Using a Plane-Wave Basis Set. *Comput. Mater. Sci.* **1996**, *6*, 15−50.

(43) Kresse, G.; Hafner, J. Ab Initio Molecular Dynamics for Liquid Metals. *Phys. Rev. B* **1993**, *47*, 558−561.

(44) Butler, K. T.; Hendon, C. H.; Walsh, A. Electronic Chemical Potentials of Porous Metal-Organic Frameworks. *J. Am. Chem. Soc.* **2014**, *136*, 2703−2706.

(45) *WMD-Group/MacroDensity: Analyse VASP Density & Potential Grids Using Python*; GitHub, 2020. https://github.com/WMD-group/MacroDensity (accessed Mar 15, 2020).

(46) Gerber, E.; Yao, Y.; Arias, T. A.; Kim, E. A. Ab Initio Mismatched Interface Theory of Graphene on $\alpha$-RuCl$_3$: Doping and Magnetism. *Phys. Rev. Lett.* **2020**, *124*, No. 106804.

(47) Tang, W.; Sanville, E.; Henkelman, G. A Grid-Based Bader Analysis Algorithm without Lattice Bias. *J. Phys.: Condens. Matter* **2009**, *21*, No. 084204.

(48) Henkelman, G.; Arnaldsson, A.; Jónsson, H. A Fast and Robust Algorithm for Bader Decomposition of Charge Density. *Comput. Mater. Sci.* **2006**, *36*, 354−360.

(49) Yu, M.; Trinkle, D. R. Accurate and Efficient Algorithm for Bader Charge Integration. *J. Chem. Phys.* **2011**, *134*, No. 064111.

(50) Zeppenfeld, A. C.; Fiddler, S. L.; Ham, W. K.; Klopfenstein, B. J.; Page, C. J. Variation of Layer Spacing in Self-Assembled Hafnium-1,10-Decanediylbis(Phosphonate) Multilayers As Determined by Ellipsometry and Grazing Angle X-Ray Diffraction. *J. Am. Chem. Soc.* **1994**, *116*, 9158−9165.

(51) Moore, D. B.; Beekman, M.; Zschack, P.; Johnson, D. C. In Synthesis of Four New Members of the $(PbSe)_{1.16}(TiSe_2)n$ (n = 1, 2, 3, and 4) Family of Ferecrystals, 2011 11th IEEE International Conference on Nanotechnology; IEEE, 2011; pp 1363−1366.

(52) Bauers, S. R.; Merrill, D. R.; Moore, D. B.; Johnson, D. C. Carrier Dilution in TiSe$_2$ Based Intergrowth Compounds for Enhanced Thermoelectric Performance. *J. Mater. Chem. C* **2015**, *3*, 10451−10458.

(53) Bauers, S.; Ditto, J.; Moore, D. B.; Johnson, D. C. Structure-Property Relationships in Non-Epitaxial Chalcogenide Heterostructures: The Role of Interface Density on Charge Exchange. *Nanoscale* **2016**, *8*, 14665−14672.

(54) Reshak, A. H.; Auluck, S. Electronic and Optical Properties of the 1 T Phases of TiS$_2$, TiSe$_2$, and TiTe$_2$. *Phys. Rev. B* **2003**, *68*, No. 245113.

(55) Wiedemeier, H.; von Schnering, H. G. Refinement of the Structures of GeS, GeSe, SnS and SnSe. *Z. Krist.* **1978**, *148*, 295−303.

(56) Beekman, M.; Cogburn, G.; Heideman, C.; Rouvimov, S.; Zschack, P.; Neumann, W.; Johnson, D. C. New Layered Intergrowths in the Sn-Mo-Se System. *J. Electron. Mater.* **2012**, *41*, 1476−1480.

(57) Alemayehu, M. B.; Falmbigl, M.; Ta, K.; Grosse, C.; Westover, R. D.; Bauers, S. R.; Fischer, S. F.; Johnson, D. C. Structural and Electrical Properties of $([SnSe]_{1+\delta})_M(NbSe_2)_1$ Compounds: Single NbSe$_2$ Layers Separated by Increasing Thickness of SnSe. *Chem. Mater.* **2015**, *27*, 867−875.

(58) Atkins, R.; Dolgos, M.; Fiedler, A.; Grosse, C.; Fischer, S. F.; Rudin, S. P.; Johnson, D. C. Synthesis and Systematic Trends in Structure and Electrical Properties of $[(SnSe)_{1.15}]_m(VSe_2)_1$, m = 1, 2, 3, and 4. *Chem. Mater.* **2014**, *26*, 2862−2872.

(59) Lygo, A. C.; Hamann, D. M.; Moore, D. B.; Merrill, D. R.; Ditto, J.; Esters, M.; Orlowicz, J.; Wood, S. R.; Johnson, D. C. Kinetically Controlled Formation and Decomposition of Metastable $[(BiSe)_{1+\delta}]_m$ $[TiSe_2]_m$ Compounds. *J. Am. Chem. Soc.* **2018**, *140*, 3385−3393.

(60) Wood, S. R.; Merrill, D. R.; Mitchson, G.; Lygo, A. C.; Bauers, S. R.; Hamann, D. M.; Sutherland, D. R.; Ditto, J.; Johnson, D. C. Modulation Doping in Metastable Heterostructures via Kinetically Controlled Substitution. *Chem. Mater.* **2017**, *29*, 773−779.

(61) Moore, D. B.; Stolt, M. J.; Atkins, R.; Sitts, L.; Jones, Z.; Disch, S.; Beekman, M.; Johnson, D. C. Structural and Electrical Properties of $(PbSe)_{1.16}TiSe_2$. *Emerging Mater. Res.* **2012**, *1*, 292−298.

(62) Moore, D. B.; Beekman, M.; Disch, S.; Zschack, P.; Häusler, I.; Neumann, W.; Johnson, D. C. Synthesis, Structure, and Properties of Turbostratically Disordered $(PbSe)_{1.18}(TiSe_2)_2$. *Chem. Mater.* **2013**, *25*, 2404−2409.

(63) Wood, S. R.; Merrill, D. R.; Falmbigl, M.; Moore, D. B.; Ditto, J.; Esters, M.; Johnson, D. C. Tuning Electrical Properties through Control of TiSe$_2$ Thickness in $(BiSe)_{1+\delta}(TiSe_2)_N$ Compounds. *Chem. Mater.* **2015**, *27*, 6067−6076.

(64) Merrill, D. R.; Sutherland, D. R.; Ditto, J.; Bauers, S. R.; Falmbigl, M.; Medlin, D. L.; Johnson, D. C. Kinetically Controlled Site-Specific Substitutions in Higher-Order Heterostructures. *Chem. Mater.* **2015**, *27*, 4066−4072.

(65) Falmbigl, M.; Alemayehu, M. B.; Merrill, D. R.; Beekman, M.; Johnson, D. C. In-Plane Structure of Ferecrystalline Compounds. *Cryst. Res. Technol.* **2015**, *50*, 464−472.

(66) Göhler, F.; Hamann, D. M.; Rösch, N.; Wolff, S.; Logan, J. T.; Fischer, R.; Speck, F.; Johnson, D. C.; Seyller, T. Electronic Structure of Designed $[(SnSe)_{1+\delta}]_m[TiSe_2]_2$ Heterostructure Thin Films with Tunable Layering Sequence. *J. Mater. Res.* **2019**, *34*, 1965−1975.

(67) Bauers, S. R.; Johnson, D. C. Designing Thermoelectric Materials Using 2D Layers. *Handbook of Solid State Chemistry*; Wiley-VCH Verlag GmbH & Co. KGaA, 2017; pp 93−122.

(68) Sheets, W. C.; Mercey, B.; Prellier, W. Effect of Charge Modulation in $(LaVO_3)_m(SrVO_3)_n$ Superlattices on the Insulator-Metal Transition. *Appl. Phys. Lett.* **2007**, *91*, No. 192102.

(69) Miyasaka, S.; Okuda, T.; Tokura, Y. Critical Behavior of Metal-Insulator Transition in La1-XSrxVO$_3$. *Phys. Rev. Lett.* **2000**, *85*, 5388−5391.

(70) Zubair Ansari, M.; Khare, N. Thermally Activated Band Conduction and Variable Range Hopping Conduction in $Cu_2ZnSnS_4$ Thin Films. *J. Appl. Phys.* **2015**, *117*, No. 025706.

(71) Huang, Y. L.; Chiu, S. P.; Zhu, Z. X.; Li, Z. Q.; Lin, J. J. Variable-Range-Hopping Conduction Processes in Oxygen Deficient Polycrystalline ZnO Films. *J. Appl. Phys.* **2010**, *107*, No. 063715.

(72) Khan, M. H.; Pal, S. Nature of Electrical Hopping Conduction and Magnetotransport Studies in the Electron Doped Manganite $Ca_{0.85}Gd_{0.15}MnO_3$. *Phys. Lett. A* **2015**, *379*, 401−406.

(73) Hill, R. M. Variable-range Hopping. *Phys. Status Solidi A* **1976**, *34*, 601−613.

(74) Edwards, P. P.; Sienko, M. J. The Transition to the Metallic State. *Acc. Chem. Res.* **1982**, *15*, 87−93.

(75) Möbius, A. The Metal-Insulator Transition in Disordered Solids: How Theoretical Prejudices Influence Its Characterization A Critical Review of Analyses of Experimental Data. *Crit. Rev. Solid State Mater. Sci.* **2019**, 1−55.

(76) Wang, Y.; Nakano, M.; Kashiwabara, Y.; Matsuoka, H.; Iwasa, Y. Transport Properties of a Few Nanometer-Thick TiSe2 Films Grown by Molecular-Beam Epitaxy. *Appl. Phys. Lett.* **2018**, *113*, No. 073101.

(77) Watson, M. D.; Beales, A. M.; King, P. D. C. On the Origin of the Anomalous Peak in the Resistivity of $TiSe_2$. *Phys. Rev. B* **2019**, *99*, No. 195142.

(78) Di Salvo, F. J.; Moncton, D. E.; Waszczak, J. V. Electronic Properties and Superlattice Formation in Semimetal $TiSe_2$. *Phys. Rev. B* **1976**, *14*, 4321.

(79) Kehoe, A. B.; Scanlon, D. O.; Watson, G. W. Nature of the Band Gap of $Tl_2O_3$. *Phys. Rev. B: Condens. Matter Mater. Phys.* **2011**, *83*, No. 233202.

(80) Monney, C.; Battaglia, C.; Cercellier, H.; Aebi, P.; Beck, H. Exciton Condensation Driving the Periodic Lattice Distortion of 1T-$TiSe_2$. *Phys. Rev. Lett.* **2011**, *106*, No. 106404.

(81) Bianco, R.; Calandra, M.; Mauri, F. Electronic and Vibrational Properties of $TiSe_2$ in the Charge-Density-Wave Phase from First Principles. *Phys. Rev. B: Condens. Matter Mater. Phys.* **2015**, *92*, No. 094107.

(82) Cazzaniga, M.; Cercellier, H.; Holzmann, M.; Monney, C.; Aebi, P.; Onida, G.; Olevano, V. Ab Initio Many-Body Effects in $TiSe_2$: A Possible Excitonic Insulator Scenario from GW Band-Shape Renormalization. *Phys. Rev. B: Condens. Matter Mater. Phys.* **2012**, *85*, No. 195111.